On critical collapse of gravitational waves

Evgeny Sorkin

Max Planck Institute for Gravitational Physics (Albert Einstein Institute)
Am Muehlenberg 1, Potsdam, 14476, Germany

E-mail: Evgeny.Sorkin@aei.mpg.de

Abstract. An axisymmetric collapse of non-rotating gravitational waves is numerically investigated in the subcritical regime where no black holes form but where curvature attains a maximum and decreases, following the dispersion of the initial wave packet. We find that near the threshold for black hole formation a curvature invariant with dimensions of length, scales as a power-law with the approximate exponent 0.38. In addition, the variation of the curvature in the critical limit is accompanied by increasing amount of echos, with nearly equal temporal and spatial periods. The scaling and the echoing patterns, and the corresponding constants are independent of the initial data and coordinate choices.

PACS numbers: 04.25.D-,04.25.dc,04.20.-q

1. Introduction

Universality, scaling and self-similarity found in critical gravitational collapse is one of the most fascinating phenomena associated with gravitational interactions. First discovered numerically by Choptuik [1] in spherically-symmetric collapse of massless scalar field, this distinctive behavior was later observed in other systems, including those with various matter contents and equations of state, diverse spacetime dimensions etc. However, while a great deal of literature has emerged on critical phenomena in spherical symmetry, only a limited number of non-perturbative studies exists in less symmetric settings, see [2] for a review.

Perhaps the simplest non-spherical system is a pure axisymmetric gravitational wave, collapsing under its own gravity. Abrahams and Evans [3] found that the mass of black holes, forming in the evolution of sufficiently strong initial waves, exhibits scaling of the form $M_{bh} \propto (a - a_*)^\beta$ in the limit when the strength parameter a tends to a_*, the threshold for black hole formation, and determined the exponent of the power-law to be $\beta \simeq 0.35 - 0.38$. They have also given less conclusive evidence of periodic echoing of the near critical solutions. Surprisingly, these results proved difficult to reproduce; in fact no other successful simulation of the axisymmetric vacuum collapse has been reported to date (see e.g. [4] for a failed attempt). However, in this paper we present new results obtained with the aid of our recent harmonic code [5].

We focus on subcritical collapse of axisymmetric non-rotating Brill waves during which black holes do not form, but where curvature grows to reach a maximum and subsequently diminishes, following the dispersion of the initial wave. Perturbative studies of the critical solutions [2, 6] suggest that the power-law scaling of characteristic quantities near the critical point should occur on both sides of the black hole formation

threshold, regardless of appearance of horizons. While this was confirmed in numerical experiments in spherical symmetry, see e.g [7, 8], it is an open question whether same is true in other situations as well. Here we demonstrate that in the axisymmetric subcritical collapse, a curvature invariant with dimensions of length follows a power-law with the exponent, $\beta = 0.385 \pm 0.015$, similar to that found by Abrahams and Evans in supercritical case. Additionally, we find that the solutions develop increasingly large numbers of echos as the critical limit is approached. Our current resolution allows observation of up to three echos around the time instant where curvature is maximal. We measure that, for example, the Riemann curvature invariant oscillates in time with the (logarithmic) period of $\Delta_\tau \simeq 1.1$, and that the logarithm of the invariant changes on each echo by nearly same amount $\Delta_r \sim \Delta_\tau \simeq 1.1$.

We verify that the scaling and echoing constants are essentially independent of initial data and specific coordinate conditions used to calculate the solutions. In contrast to spherically symmetric collapse, where the greatest curvature is always at the origin, the evolution of the axisymmetric waves is more complicated and the spacetime location of the maximum depends strongly on the geometry of the initial data. We evolved series of initial data where curvature attained a maximum along equatorial rings of various radii centered at the axis. We found that despite very different ensuing dynamics in these cases, the near critical scaling and echoing patterns are universal, and the corresponding constants are comparable.

In the next section we briefly describe the initial value problem for constructing the axisymmetric vacuum asymptotically flat spacetimes without angular momentum; the details of the equations, gauge conditions and our numerical code are found in [5]. Section 3 is devoted to the results and numerical tests. We summarize our findings, discuss limitations of the current method and outline perspectives in the concluding section 4.

2. The equations and a method of their solution

We are interested in solving the vacuum Einstein equations

$$R_{\mu\nu} = 0, \tag{1}$$

where $R_{\mu\nu}$ is the Ricci tensor. We consider axisymmetric asymptotically flat spacetimes without angular momentum, and assume they can be foliated by a family of spacelike hypersurfaces, starting with the initial surface at $t = 0$, where the spatial metric and its normal derivatives are chosen to satisfy the constraints (Gauss-Codazzi equations).

The most general metric adapted to the symmetries of the problem can be written using the cylindrical coordinates

$$ds^2 = g_{ab}\, dx^a\, dx^b + r^2 e^{2\,S} d\phi^2, \tag{2}$$

where the seven metric functions—g_{ab}, $a, b = 0, 1, 2$ and S—depend only on t, r and z. ‡ In order to solve the field equations (1) we employ the Generalized Harmonic (GH) formalism [9, 10, 11], adopted to the axial symmetry in [5]. To this end we define the GH constraint,

$$C^a \equiv -\Box x^a + H^a = -\Gamma^a_{\alpha\beta} g^{\alpha\beta} + H^a = 0, \tag{3}$$

‡ While Greek indices range over $t, r, z, \phi = 0, 1, 2, 3$, Latin indices run over $0, 1, 2$.

where $\Gamma^a_{\alpha\beta}$ are Christoffel symbols, and the "source functions" $H^a = H^a(x, g)$ depend on coordinates and the metric (but do not on the metrics's derivatives) and are arbitrary otherwise. We than modify the Einstein equations:

$$R_{\mu\nu} - C_{(\mu;\nu)} = 0, \tag{4}$$

that now become a set of quasilinear wave equations for the metric components of the form $g^{\alpha\beta} g_{\mu\nu,\alpha\beta} + \ldots = 0$, where ellipses designate terms that may contain the metric, the source functions and their derivatives.

Fixing the coordinate freedom in the GH language amounts to specifying the source functions, and we choose those by requiring that the spatial coordinates satisfy damped wave equations, while the time coordinate is well behaved [12, 5]. A particular example of these conditions [12], that we use here, can be written in terms of the kinematic ADM variables as

$$H^{DW}_a = 2\,\mu_1\,\log\left(\frac{\gamma^{1/2}}{\alpha}\right)\,n_a - 2\,\mu_2\,\alpha^{-1}\,\gamma_{ai}\,\beta^i, \tag{5}$$

where $n_\mu = (-g^{00})^{-1/2}\partial_\mu\, t$ is the unit normal to the spatial hypersurfaces of constant time, α is the lapse, β^i is the shift, $\gamma_{ab} = g_{ab} + n_a n_b$ is the spatial metric, $\gamma = (g_{11}\, g_{22} - g_{12}^2)\, \exp(S)$, and μ_1 and μ_2 are parameters.

The initial data is given at $t = 0$, where we choose the initial spatial metric to be in the form of the Brill-wave [13]

$$ds_3^2 = \psi^4(r, z)\left[e^{2\,r\,B(r,z)}\left(dr^2 + dz^2\right) + r^2\,d\phi^2\right], \tag{6}$$

with

$$B(r, z) \equiv a\,r \exp\left(-\frac{r^2}{\sigma_r^2} - \frac{z^2}{\sigma_z^2}\right), \tag{7}$$

where σ_r, σ_z and a are parameters.

We further assume time-symmetry, in which case the momentum constraint identically vanishes at $t = 0$, while the Hamiltonian constraint becomes the elliptic equation for ψ

$$\left(\partial_r^2 + \frac{1}{r}\partial_r + \partial_z^2\right)\psi = -\frac{1}{4}\psi\, r\,\left(\partial_r^2 + \frac{2}{r}\partial_r + \partial_z^2\right) B, \tag{8}$$

which is solved subject to regularity conditions at the axis, equatorial reflection symmetry, and asymptotic flatness boundary conditions:

$$\partial_z\psi(r, 0) = 0, \quad \partial_r\psi(0, z) = 0, \quad \psi(r, \infty) = \psi(\infty, z) = 1. \tag{9}$$

We assume initially harmonic coordinates, $H^a = 0$ and choose the initial lapse $\alpha(t = 0, r, z) \equiv g_{00}^{1/2}(t = 0, r, z) = 1$.

Having specified the initial data we integrate the equations (4) forward in time, imposing asymptotic flatness and regularity at the axis, $r = 0$. For simplicity, we restrict attention to the spacetimes having equatorial reflection symmetry. The highlights of our finite-differencing approximation (FDA) numerical code [5] that we employ to solve the equations include:

- An introduction of a new variable that facilitates axis regularization. While elementary flatness at the axis implies that each metric component has either to vanish or to have vanishing normal derivative at that axis, requiring absence of a conical singularity at $r = 0$ results in the additional condition: $g_{11}(t, 0, z) =$

$\exp[2\,S(t,0,z)]$. Therefore, at $r=0$ we essentially have three conditions on the two fields S and g_{11}. While in the continuum, and given regular initial data, the evolution equations will preserve regularity, in a FDA numerical code this will be true only up to discretization errors. Our experience shows that the number of boundary conditions should be equal to the number of evolved variables in order to avoid regularity problems and divergences of a numerical implementation. We deal with this regularity issue by defining a new variable

$$\lambda \equiv \frac{g_{11} - e^{2\,S}}{r}, \tag{10}$$

that behaves as $\lambda \sim O(r)$ at the axis, and use it in the evolution equations instead of S. This eliminates the overconstraining and completely regularizes the equations. Crucially, the hyperbolicity of the GH system is not affected by the change of variables.

- Constraint damping. The constraint§ equations, $C_\mu = 0$, are not solved in the free evolution schemes like ours, except at the initial hypersurface. While one can show that in the continuum the constraints are satisfied at all times, in FDA codes small initial violations tend to grow and destroy convergence. A method that we use to damp constraints violations consists of adding to the equations (4) the term of the form [15, 16],

$$Z_{\mu\nu} \equiv \kappa \left(n_{(\mu} C_{\nu)} - \frac{1}{2} g_{\mu\nu}\, n^\beta\, C_\beta \right), \tag{11}$$

  where κ is a parameter. We note that $Z_{\mu\nu}$ contains only first derivatives of the metric and hence does not affect the principal (hyperbolic) part of the equations.
- A spatial compactification is introduced in both spatial direction by transforming to the new coordinates $\bar{x} = x/(1+x), \bar{x} \in [0,1], x \in [0,\infty)$, where x stands for either r or z. The advantage of this scheme is that asymptotic flatness conditions $g_{\mu\nu} = \eta^{Mink}_{\mu\nu}$ at the spatial infinity are exact.
- We use Kreiss-Oliger-type dissipation in order to remove high frequency discretization noise. ‖ An additional role of the dissipation is to effectively attenuate the unphysical back reflections from the outer boundaries, resulting from the loss of numerical resolution there. This allows using compactification meaningfully [11, 17].

In order to characterize the spacetimes that we construct, we use the Brill mass [13], computed at the initial time-slice,

$$M = \int \left[\left(\partial_r \log\psi\right)^2 + \left(\partial_z \log\psi\right)^2 \right] r\, dr\, dz, \tag{12}$$

which—we verify—coincides with the ADM mass. For the purpose of quantifying the strength of the gravitational field we calculate the Riemann curvature invariant having dimension of inverse length,

$$I \equiv (R_{\alpha\beta\mu\nu} R^{\alpha\beta\mu\nu})^{1/4} \tag{13}$$

§ It can be shown that the standart Hamiltonian and momentum constraints are equivalent to the GH constraints [14].

‖ i.e. the noise with frequency of order of the inverse of the mesh-spacing

$\sigma_r,\ \sigma_z$	$\mu_1,\ \mu_2$	h	a_*	M_*	ρ_*	τ_*
1.0, 1.0	0.1, 1.1	1/200	5.985 ± 0.005	0.969	0.2	1.5
1.0, 1.0	0.12, 1.17	1/300	6.20021 ± 0.00001	1.04	0.15	1.46
1.0, 1.0	0.2, 1.0	1/400	6.273 ± 0.001	1.06	0.2	1.45
0.9, 1.3	0.3, 0.9	1/300	7.3079082 ± 0.0000002	1.12	0.23	1.59
0.9, 1.3	0.3, 0.9	1/128, 2l	7.246067 ± 0.000002	1.1	0.23	1.64
0.9, 1.3	0.3, 0.9	1/128, 4l	6.9401 ± 0.0002	1.0	0	1.51
0.8, 1.3	0.2, 1.1	1/300	6.786 ± 0.004	0.607	0.1	3
0.7, 1.5	0.2, 1.1	1/300	8.21 ± 0.01	0.593	0.0	3.2

Table 1. The parameters of the initial data a, σ_r, σ_z, and numerical and gauge constants determine the total mass, the threshold amplitude and the "accumulation locus". While the upper margin in the listed critical amplitudes corresponds to formation of a black hole, the lower margin corresponds to a regular spacetime. The radial position of the accumulation locus is measured in terms of the circumferential radius (15); the proper time at that location is measured in the units of the total mass. $2l$ and $4l$ indicate the amount of the AMR levels used in these cases; other simulations are unigrid.

at various locations, and in certain experiments we follow its evolution in the proper time at that location (r, z),

$$\tau(t, r, z) \equiv \int_0^t \alpha(t', r, z) dt'. \tag{14}$$

We also use the circumferential radius

$$\rho \equiv r\, e^S. \tag{15}$$

3. Results

The initial data (6,7) are characterized by the amplitude a and the "shape" parameters σ_r and σ_z, which define the mass of the data and their "strength", namely the tendency to collapse and form a black hole. For a given amplitude and fixed $\sigma_r + \sigma_z = const$, the data with larger σ_z/σ_r are stronger (see also [18, 19]). In addition, by varying the shape parameters at fixed gauge, we can control the spacetime locations where curvature evolves to a maximum or where an apparent horizon first forms. In our experiments we use several sets of σ_r and σ_z, and adjust the strength of the initial wave by tuning its amplitude.

The initial data are numerically evolved forward in time. We use grids with similar mesh-sizes in both spatial dimensions $h_r = h_z = h$, and time-steps of $h_t = 0.04\, h - 0.05\, h$. Usually our fixed grids consist of 200, 250, 300 or 400 points, uniformly covering the compactified spatial directions. We also experiment with adaptive mesh refinement (AMR), provided by the PAMR/AMRD software [20]. In this case we use two or four refinement levels, and the base mesh with the resolution of $h = 1/128$. The Kreiss-Oliger dissipation parameter is typically $\epsilon_{KO} = 0.5 - 0.85$, with larger values used on finer grids and stronger initial data; and the constraint damping parameter in (11) is $\kappa = 1.4 - 1.7$. The gauge fixing parameters (5) in the ranges $\mu_1 \simeq 0.1 - 0.3$ and $\mu_2 \simeq 0.9 - 1.2$, usually gave stable, sufficiently long evolutions.

The system is weakly gravitating for small amplitudes, in which cases the initial wave packet ultimately disperses to infinity. However, for amplitudes above certain threshold, a_*, the wave collapses to form a black hole, signaled by an apparent horizon.

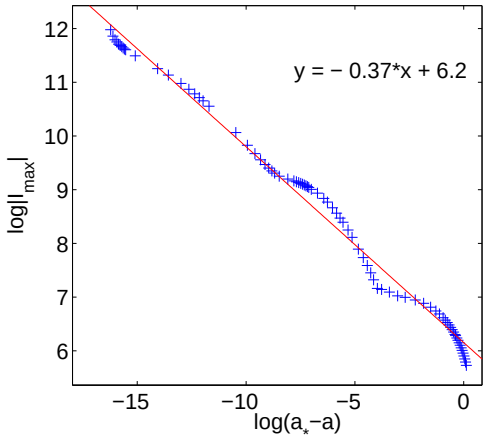

Figure 1. A logarithm of the maximal Riemann invariant (13) as a function of the distance from the critical amplitude, $a_* - a$, in the simulations with $\sigma_r = 0.9$, $\sigma_z = 1.3$, and the fixed resolution $h = 1/300$. The critical amplitude in this case is $a_* = 7.3079082$, and the maximal curvature is $|I_{max}| \sim 10^5$ in the units of the total mass. The linear fit to the data (solid line) has the slope $\beta \simeq -0.37$. Notice the (quasi-) periodic "wiggle" of the data points about the straight line.

In subcritical spacetimes we can define the "accumulation locus" where curvature attains a global maximum before decaying. In our coordinates (5), and for our initial data (where the ratio between σ's never exceeds five) the position of this maximum (t_*, r_*, z_*) is always along the equator $z_* = 0$.

The threshold amplitude for black hole formation depends on the initial data and gauge and numerical parameters. Table 1 records critical amplitudes, masses and the spacetime positions of the accumulation locus for a few examples of the data sets which we have evolved. In contrast to spherically-symmetric collapse, where accumulation locus is always the origin, in axial symmetry the situation is more complicated. For instance, we find that for $\sigma_r = \sigma_z = 1$ the curvature achieves a maximum at $\tau_* \simeq 1.46\, M_*$ along a ring of the approximate radius $\rho \sim 0.2$, while for $\sigma_r = 0.7, \sigma_z = 1.5$ the accumulation locus is the origin, and the maximum is approached at a later instant, $\tau_* \simeq 3.2\, M_*$. As described next, there is a power-law scaling of curvature in the limit $a/a_* \to 1$, and we find its onset starting from relatively large values of $a_*/a - 1 \sim 10^{-3}$, for all resolutions better than $h = 1/200$. ¶ However, it turns out that the data calculated in fixed-mesh simulations with $h \gtrsim 1/250$ is somewhat noisy and dependent on details of the numerics, to provide a reliable estimate of the scaling exponent.

The scaling can be envisaged by plotting the maximal value of the Riemann curvature invariant (13) as a function of the parametric distance from the critical amplitude $a_* - a$; this is shown in Fig. 1. Each point here represents the global maximum $|I_{max}|$ computed during evolutions defined by $\sigma_r = 0.9$ and $\sigma_z = 1.3$, and the numerical parameters: $h = 1/300, h_t/h = 0.04, \mu_1 = 0.3, \mu_2 = 0.9, \kappa = 1.7, \epsilon = 0.6$. The solid line represents the least-squares linear fit to the data. The slope of the line,

¶ For comparison, in scalar field collapse the signatures of near-critical scaling do not appear before $a_*/a - 1 \lesssim 10^{-8}$.

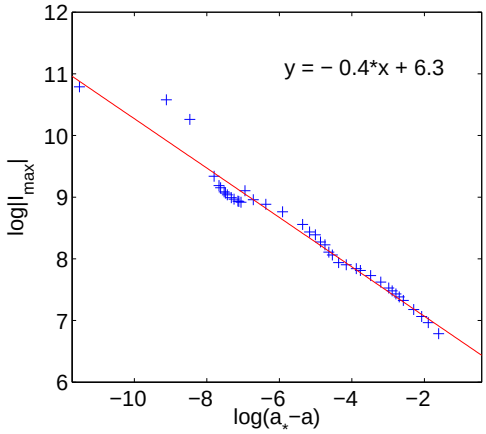

Figure 2. A plot similar to Fig. 1, but obtained with different parameters: $\sigma_r = \sigma_z = 1$ and the resolution $h = 1/300$. In this case the critical amplitude is $a_* = 6.20021$. Remarkably, the slopes of the linear fits in both figures agree to within 8%.

$\beta \simeq -0.37$, is in agreement with the exponent of the black-holes' mass scaling, [+] found in supercritical collapse by Abrahams and Evans [3]. The data depicted in Fig. 2 were obtained with a differently shaped initial wave, $\sigma_r = \sigma_z = 1$, and the parameters $h = 1/300, h_t/h = 0.05, \mu_1 = 0.12, \mu_2 = 1.17, \kappa = 1.7, \epsilon = 0.8$. The threshold amplitude in this case is found with somewhat lesser accuracy, $a_* = 6.20021 \pm 0.00001$. However, the data is still fitted well with a straight line whose slope, $\beta \simeq -0.4$, coincides with the exponent in Fig. 1 to within 8%.

It is remarkable that despite the evolutions of the initial waves shown in Figs. 1 and 2 are dramatically different, the maximal curvatures in both cases follow a power-law with similar exponents. We verify that the same scaling again appears in simulations with other shape parameters and in all cases that resulting exponent is consistently in the range $\beta \simeq 0.37 - 0.4$. In addition, the scaling exponent does not leave this range when we use coordinate conditions with different choices of μ's in (5) (see e.g. Figs. 1 and 2). While this does not test the rigidity of β with respect to all possible coordinate conditions, this demonstrates relative consistency of the exponent within the large family of the gauges (5). We conclude that in the critical limit the maximal curvature predominantly scales as $|I_{max}| \propto (a_* - a)^{-\beta}$, with $\beta = 0.385 \pm 0.015$.

The distribution of data points in Figs. 1 and 2 has a striking property, namely the data "wiggle" about the linear fit. We note that similar wiggle was also observed in near critical collapse of scalar field. In that case it was attributed [22] to the periodic self-similarity found in that system, where the critical solution, Z_*, repeats on itself after a discrete period Δ: $Z_*(\tau, r) = Z_*(\tau\, e^{\Delta}, r\, e^{\Delta})$. Besides, [22] found that the period of the wiggle is $\Delta/(2\,\beta)$, and thus may, in principle, allow calculating the self-similarity scale Δ by measuring the slope and the period of the wiggle in a plot like ours Figs. 1 and 2. Although, the quasi-periodic fluctuations of the points about the linear fit in these figures do signal discrete self-similarity, our current data

[+] Note that our exponent is negative since the dimensions of I are inverse length, while black hole mass has dimensions of length.

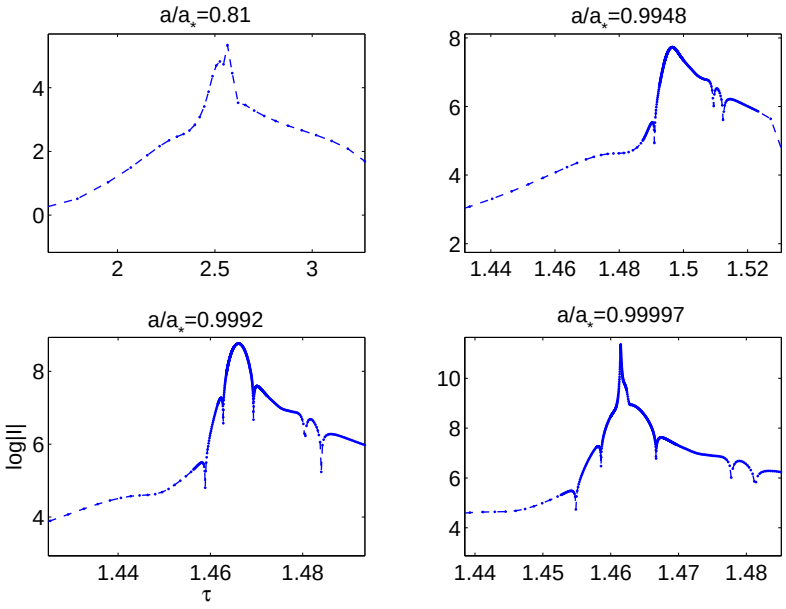

Figure 3. The dynamics of the logarithm of the Riemann invariant as a function of the proper time $\tau(r_*)$ for several values of a/a_*. The variation of I toward the accumulation, τ_*, and away from it is accompanied by oscillations, whose number grows in the limit $a \to a_*$. The double dip in top right panel at about $\tau \simeq 1.51$ and in bottom panels near $\tau \simeq 1.48$ is a result of the interference between the main and a secondary reflection off the axis.

are insufficiently accurate and have too short a span to provide more quantitative estimate of the wiggle period, beyond a very rough value of anything between two and four.

Independent, and more direct signatures of discrete self-similarity are obtained by examining the detailed behavior of the curvature when $a \to a_*$. It turns out that in this limit, in addition to that I attains increasingly larger maxima, the temporal variation of I is also accompanied by increasing amount of oscillations. This is illustrated in Fig. 3, which shows how I develops in the proper time, calculated at the position of the maximum, for a sequence of a's. It is apparent from these plots that the amount of fluctuations (indicated by the peaks or inflection points) grows from one to three in the limit $a/a_* \to 1$ on both sides of the accumulation locus. Such an oscillatory behavior is again reminiscent of the "echoing" in critical spherical collapse of scalar field (see e.g. Fig. 5 in [8] and Fig. 7 in [21]) and we interpret it as evidence of periodic self-similarity in our system as well.

Like the power-law scaling of the maximal curvature, the echoing of our solutions in the near critical limit is independent of specific gauges or particular initial data sets. This is demonstrated in Fig. 4, which depicts temporal evolutions of the Riemann invariant and the lapse function found in simulations of the initial data characterized by $\sigma_r = 0.9$, $\sigma_z = 1.3$, the gauge constants $\mu_1 = 0.3$, $\mu_2 = 0.9$, and the amplitude $a = 6.94$. The functions in left panels were computed using 2 levels of AMR, and the other panels were generated using 4 levels of AMR; in both cases the base-level

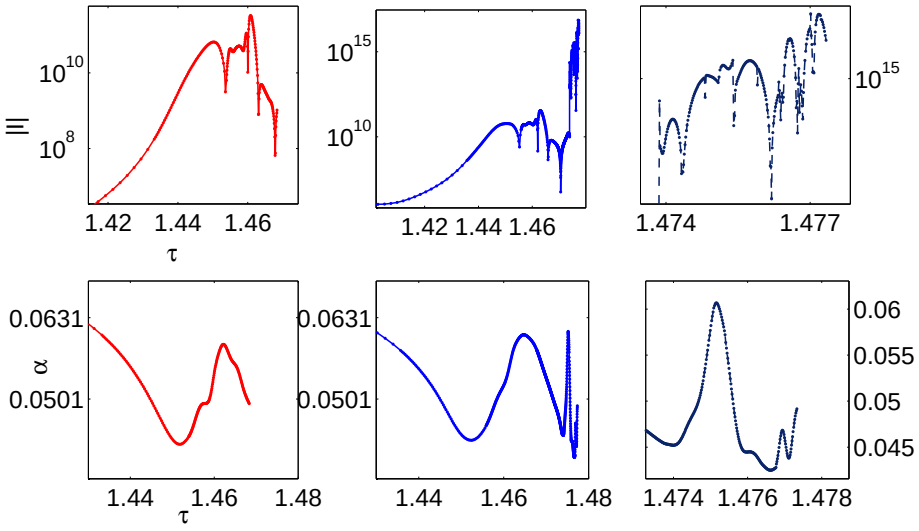

Figure 4. The echoing pattern obtained in the evolution of the initial data sets with $\sigma_r = 0.9$, $\sigma_z = 1.3$ and $a = 6.940$. Left panels show the low resolution runs that use 2 levels of AMR, with the base $h = 1/128$, other panels were obtained using 4 AMR levels with the same base; the rightmost panels is the zooming of the late time behavior shown in middle panels. While the lower resolution runs diverge at $\tau \simeq 1.47$, the higher resolution runs extend beyond that, allowing to calculate additional echos. Notice that I has sharper and easier to identify features than α.

resolution is $h = 1/128$. The figure shows that the dynamics in this case is considerably more complicated than in the $\sigma_r = \sigma_z$ runs (see Fig. 3), involving multiple scatterings and interferences of the initial and secondary waves. As expected, in most cases higher resolution simulations run longer and allow computing more oscillations. Notice that the shapes of the curves in left and middle panels in Fig. 4 are essentially identical until $\tau \sim 1.47$. However, the lower resolution runs blow up around that time due to formation of a singularity, while the higher resolution evolutions continue beyond that and show additional echos accumulating near $\tau_* \simeq 1.477 M_*$, just before our numerics fails. The spatial position of the accumulation locus in this case is the origin. Interestingly we find a different accumulation locus along $\rho_* \simeq 0.23$ for another critical amplitude of $a_* = 7.246067$, see Table 1, which is detectable in the low resolution simulations as well. Is is quite remarkable than that the resulting scaling and echoing constants turn out to be identical in both cases, even though the total masses of the spacetimes, the accumulation loci and the details of evolution are dramatically different.

In order to estimate the period of the echos we plot in Fig. 5 the temporal variation of I computed in the evolution of the initial data set, having $\sigma_r = \sigma_z = 1$, $a = 6.2002$. By measuring the distances between the peaks or inflection points—marked by arrows in Fig. 5—we find that the curvature fluctuates in time with the logarithmic period $\Delta_\tau = 0.95 \pm 0.15$ and that on each echo the logarithm of I varies by approximately $\Delta_r \simeq 1.1 \pm 0.1$. We note that both periods agree within the error-bars. A similar Fig. 6 shows the dynamics of I against $\tau_* - \tau$, that was obtained

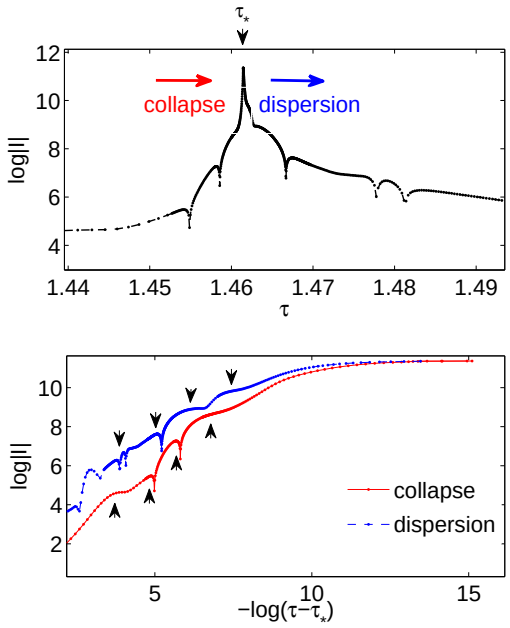

Figure 5. The typical temporal variation of the curvature invariant I near the accumulation locus is oscillatory in time. Shown is the evolution of the initial data with $\sigma_r = \sigma_z = 1$ and $a/a* = 0.999998$. On each oscillation $\log|I|$ varies by $\Delta_r \simeq 1.1 \pm 0.1$, which is close to the time period $\Delta_\tau \simeq 0.95 \pm 0.15$ of the four oscillations around τ_*.

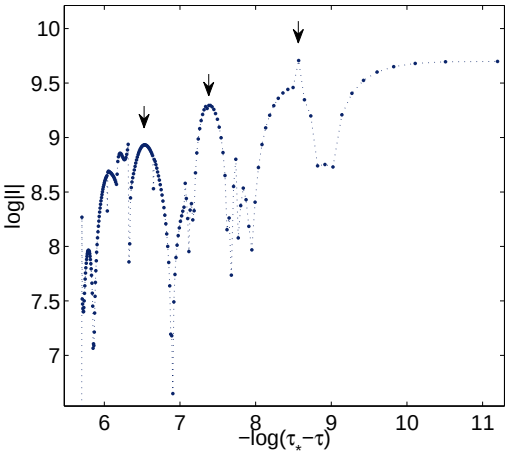

Figure 6. The variation of I obtained in a 4-level AMR simulations initialized by $\sigma_r = 0.9$, $\sigma_z = 1.3$, and $a/a* \simeq 0.99997$. The variation of $\log|I|$ on each oscillation (marked by arrows) is nearly equal to the temporal period of the echos, $\Delta_r \simeq \Delta_\tau \simeq 1.1$.

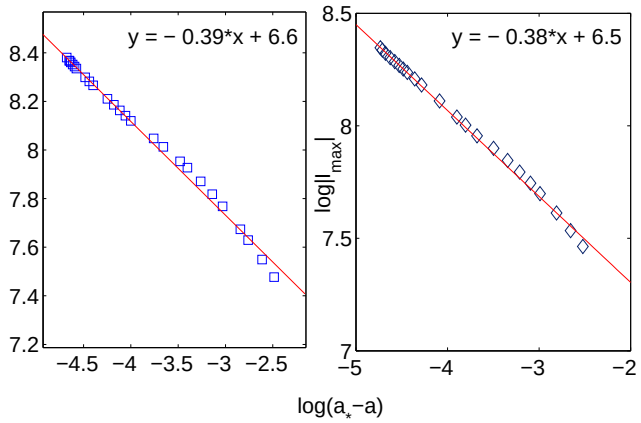

Figure 7. The logarithm of $|I_{max}|$ obtained in simulations with two distinct sets of the damping and dissipation constants: $\kappa = 1.4, \epsilon_{KO} = 0.75$ (right panel), and $\kappa = 1.5, \epsilon_{KO} = 0.85$ (left panel). We use same resolution of $h = 1/300$, and all other equal parameters. The difference in β's in this case is less than 3%, indicating the quality of our numerics.

in simulations with 4 levels of AMR, $\sigma_r = 0.9$, $\sigma_z = 1.3$, and $a = 6.940$, shown in right panels in Fig. 4. * Although the resulting dynamics is quite complicated, featuring multiple scatterings and interferences, there are 3 prominent peaks—marked by the arrows in Fig. 6—that can be identified as echos. Their temporal period is $\Delta_\tau = 1.10 \pm 0.04$, and on each echo the logarithm of $|I|$ grows by a comparable amount $\Delta_r = 1.12 \pm 0.06$. We note that these numbers are in a good agreement with the periods computed in Fig. 5.

The echoing is not specific to the curvature invariant I, other metric functions oscillate as well. However, while the echoes of I are signalled by the sharp peaks the fluctuations of metric components are typically milder, showing up as inflection points (see bottom panels in Fig. 4). This makes I a superior quantity for the purpose of measuring the echoing periods. Although we mainly discussed variations of I at the location of its global maximum, we verified that curvature develops echoes in other locations as well, where, however, the amount of the echos and their amplitude is generally smaller than around the accumulation locus.

We conclude this section by briefly discusing the accuracy of our code. While the consistency of the scaling exponents obtained in simulations with a whole different set of parameters (see e.g. Figs. 1 and 2) indicates robustness of β, the overall accuracy of our code can be tested by changing only the numerical parameters. To this end we performed simulations with different damping and the Kreiss-Oliger dissipation constants κ and ϵ_{KO}, and otherwise similar parameters. Fig. 7 shows that β's computed in two sets of simulations defined by $\kappa = 1.4, \epsilon_{KO} = 0.75$, and $\kappa = 1.5, \epsilon_{KO} = 0.85$ differ by less than 3%.

* The evolution of this initial data diverges soon after the accumulation at about $\tau \simeq 1.477 M_*$, due to imperfections of our AMR numerics. Hence only the collapse stage of the evolution is shown in this figure.

4. Discussion

We found strong evidence that in subcritical non-rotating axisymmetric vacuum collapse curvature exhibits a power-law scaling as a function of parametric distance from the threshold for black hole formation. We numerically evolved several sets of initial Brill-waves defined by fixed σ_r and σ_z, and by a tunable amplitude, a, and checked that in the limit $a \to a_*$, $|I_{max}| \propto (a_* - a)^{-\beta}$ with roughly the same exponent as that computed in supercritical regime by Abrahams and Evans [3], see Figs. 1 and 2. We verified that the exponent is relatively insensitive to variations in the initial data and coordinate conditions. Since our method differs substantially from that in [3], the good agreement of the exponents in both cases indicates robustness of the value $\beta \simeq 0.35 - 0.4$. Moreover, this lands support to the analysis of [2, 6], suggesting in particular, that quantities with same length dimensions—such as the black hole mass in [3] and the inverse curvature invariant I_{max}^{-1} here—scale identically.

There is evidence that the near critical solutions are periodically self-similar. Specifically, we observe that in the limit $a \to a_*$ the curvature invariant I undergoes increasingly large number of oscillations, whose period in the proper time is approximately equal to the rate of variation of the curvature on each echo $\Delta_\tau \simeq \Delta_r \simeq 1.1$, see Figs. 3, 5 and 6. We note that the echoing periods reported in [3], $\Delta \sim 0.6$, differ from ours, which are roughly twice larger in magnitude. However, there is no inconsistency here since the period of any specific quantity will typically depend on the particular combinations of the metric and derivatives, comprising it (for instance, the quantity $\partial^2\Psi/\partial\tau^2$ is twice more variable than Ψ). An independent, if circumstantial, signature of discrete self-similarity is the distinctive "wiggle" of the data points about the leading power-law scaling of $|I_{max}|$, see Figs. 1 and 2, since exactly this kind of behavior is expected in the periodically self-similar systems [22].

An obvious limitation of the current simulations is their maximal resolution. Even though a relatively moderate numerical resolutions of $h \simeq 1/300 - 1/1000$ have already provided fruitful insights into the critical behavior, higher resolutions are needed in order to compute the scaling and echoing constants more accurately. We expect that much closer approach to threshold will be required. This should create a longer span of data, enabling a greater accuracy of linear fits in the plots like Fig. 1 and 2, which, in turn, will allow unambiguous computation of β and of the wiggle period. A closer approach $a \to a_*$ should also multiply the number of the echoes, allowing a better estimate on their periods. Clearly, using numerical meshes of fixed size is not practical for probing the limit $a \to a_*$, rather AMR approach should be used. While we have already experimented with that, our runs often develop premature instabilities since in the near critical limit the system tends to be extremely sensitive to numerical and gauge parameters. We are currently improving our code in order to locate the optimal parameter settings, which will enable us to edge the critical limit, the results of that study will be reported elsewere.

Acknowledgments

The computations were performed on the Damiana cluster of the AEI.

References

[1] M. W. Choptuik, "Universality And Scaling In Gravitational Collapse Of A Massless Scalar Field," Phys. Rev. Lett. **70**, 9 (1993).

[2] C. Gundlach and J. M. Martin-Garcia, "Critical phenomena in gravitational collapse," Living Rev. Rel. **10**, 5 (2007)

[3] A. M. Abrahams and C. R. Evans, "Critical behavior and scaling in vacuum axisymmetric gravitational collapse," Phys. Rev. Lett. **70**, 2980 (1993), A. M. Abrahams and C. R. Evans, "Universality in axisymmetric vacuum collapse," Phys. Rev. D **49**, 3998 (1994).

[4] M. Alcubierre, G. Allen, B. Bruegmann, G. Lanfermann, E. Seidel, W. M. Suen and M. Tobias, Phys. Rev. D **61**, 041501 (2000) [arXiv:gr-qc/9904013].

[5] E. Sorkin, "An axisymmetric generalized harmonic evolution code," Phys. Rev. D **81**, 084062 (2010) [arXiv:0911.2011 [gr-qc]].

[6] T. Koike, T. Hara and S. Adachi, "Critical behavior in gravitational collapse of radiation fluid: A Renormalization group (linear perturbation) analysis," Phys. Rev. Lett. **74**, 5170 (1995)

[7] D. Garfinkle and G. C. Duncan, "Scaling of curvature in sub-critical gravitational collapse," Phys. Rev. D **58**, 064024 (1998)

[8] E. Sorkin and Y. Oren, "On Choptuik's scaling in higher dimensions," Phys. Rev. D **71**, 124005 (2005) [arXiv:hep-th/0502034].

[9] H. Friedrich, "Hyperbolic Reductions For Einstein's Equations," Class. Quant. Grav. **13**, 1451 (1996).

[10] D. Garfinkle, "Harmonic coordinate method for simulating generic singularities," Phys. Rev. D **65**, 044029 (2002)

[11] F. Pretorius, "Numerical Relativity Using a Generalized Harmonic Decomposition," Class. Quant. Grav. **22**, 425 (2005)

[12] L. Lindblom and B. Szilagyi, "An Improved Gauge Driver for the GH Einstein System," Phys. Rev. D **80**, 084019 (2009) M. W. Choptuik and F. Pretorius, "Ultra Relativistic Particle Collisions," Phys. Rev. Lett. **104**, 111101 (2010)

[13] D. R. Brill, "On the positive definite mass of the Bondi-Weber-Wheeler time-symmetric gravitational waves," Annals Phys. **7**, 466 (1959).

[14] L. Lindblom, M. A. Scheel, L. E. Kidder, R. Owen and O. Rinne, "A New Generalized Harmonic Evolution System," Class. Quant. Grav. **23**, S447 (2006)

[15] C. Gundlach, J. M. Martin-Garcia, G. Calabrese and I. Hinder, "Constraint damping in the Z4 formulation and harmonic gauge," Class. Quant. Grav. **22**, 3767 (2005) [arXiv:gr-qc/0504114].

[16] F. Pretorius, "Simulation of binary black hole spacetimes with a harmonic evolution scheme," Class. Quant. Grav. **23**, S529 (2006) [arXiv:gr-qc/0602115].

[17] E. Sorkin and M. W. Choptuik, "Generalized harmonic formulation in spherical symmetry," Gen. Rel. Grav. **42**, 1239 (2010) [arXiv:0908.2500 [gr-qc]].

[18] A. M. Abrahams, K. R. Heiderich, S. L. Shapiro and S. A. Teukolsky, "Vacuum Initial Data, Singularities, And Cosmic Censorship," Phys. Rev. D **46**, 2452 (1992).

[19] D. Garfinkle and G. C. Duncan, "Numerical evolution of Brill waves," Phys. Rev. D **63**, 044011 (2001) [arXiv:gr-qc/0006073].

[20] Parallel Adaptive Mesh Refinement (PAMR) and Adaptive Mesh Refinement Driver (AMRD), `http://laplace.phas.ubc.ca/Group/Software.html`.

[21] R. S. Hamade and J. M. Stewart, "The Spherically symmetric collapse of a massless scalar field," Class. Quant. Grav. **13**, 497 (1996) [arXiv:gr-qc/9506044].

[22] C. Gundlach, "Understanding critical collapse of a scalar field," Phys. Rev. D **55**, 695 (1997) S. Hod and T. Piran, "Fine-structure of Choptuik's mass-scaling relation," Phys. Rev. D **55**, 440 (1997)